Spatially Resolved Laser-Induced Modification Raman Spectroscopy for Probing the Microscopic Structural Variations in the Quaternary Alloy $Cu_2ZnSnSe_4$

Qiong Chen,[1] Sergio Bernardi,[2] and Yong Zhang[1,*]

[1]*Department of Electrical and Computer Engineering, and Energy Production and Infrastructure Center (EPIC), The University of North Carolina at Charlotte, Charlotte, North Carolina 28223, USA*

[2]*Semiconductor Materials Specialist, C.so Trapani 10, 10139 Turin, Italy*

(Received 7 January 2017; revised manuscript received 4 July 2017; published 14 September 2017)

While producing comparable efficiencies and showing similar properties when probed by conventional techniques, such as Raman spectroscopy, photoluminescence, and x-ray diffraction, two thin-film solar-cell materials with complex structures, such as quaternary compound $Cu_2ZnSnSe_4$ (CZTSe), may, in fact, differ significantly in their microscopic structures. In this work, laser-induced-modification Raman spectroscopy coupled with high spatial resolution and high-temperature capability is demonstrated as an effective tool to reveal the existence of microscopic scale variations between nominally similar alloys and, thus, to obtain additional structure information beyond what the conventional characterization techniques can offer. Specifically, CZTSe films prepared by sputtering and coevaporation methods that exhibit similar Raman and XRD features are found to behave very differently under high laser power and high-temperature Raman probe because the difference in their microscopic structures leads to different structure modifications in response to the external stimuli, such as light illumination and temperature. They are also shown to undergo different degrees of plastic changes and have different thermal conductivities as revealed by spatially resolved Raman spectroscopy. This technique provides a convenient way to assess and compare materials and provides complementary information for other structural characterization techniques, such as TEM and XRD.

DOI: 10.1103/PhysRevApplied.8.034008

I. INTRODUCTION

Raman spectroscopy is an effective tool for chemical composition and structural analyses of materials, assuming that the probe light intensity is sufficiently weak so that no structural change has been induced by the perturbation. While Raman spectroscopy probes the material structure through revealing the vibrational fingerprints of the material, transmission electron microscopy (TEM) is generally considered to be a more direct probe for the material structure. However, the probing volume of TEM tends to be small, typically of the order of a few tens of nanometers, which places a severe limit on the characterization efficiency when we need to have macroscopic scale structural information of an inhomogeneous material. Two extreme versions of laser spectroscopy techniques have been developed for a larger-volume structural analysis. One is called laser-induced-breakdown spectroscopy [1], which uses a highly energetic laser pulse as the excitation source to excite and atomize the sample and then measures the light emission of the atoms to determine the chemical composition of the material. In the process, the material is ablated at the excitation site. The other one is called femtosecond-laser tomography [2,3], which also uses a highly energetic ultrafast laser pulse to assist the evaporation of atoms, then time-of-flight mass spectrometry equipped with position-sensitive detectors determines the element numbers of the analyzed atoms and their spatial distribution in the sample. These two laser-based material analysis techniques are destructive and do not offer the chemical bonding information when the atoms are in the material. In contrast, the "high-power" (HP) Raman spectroscopy, as a special form of laser-induced-modification spectroscopy, uses a tightly focused continuous-wave laser with a power density that is just high enough to induce a local structural change but usually without major material ablation and measures the change in Raman features compared to the spectrum before the illumination under "low power" (LP). Performing spatially resolved Raman mapping on an as-grown material can already reveal composition and/or structural variations in the sample. However, the HP Raman spectroscopy can provide additional information beyond that obtainable from the conventional technique. For instance, some structural or chemical fluctuations are too feeble to be detectable or distinguishable in the as-grown sample or between different ones but are signified after being modified by the HP illumination. The appropriate power levels of "HP" and "LP" depend rather sensitively on the specific material of interest [4]. The application of the HP Raman spectroscopy can reveal some subtle but important structural differences in

*Corresponding author.
yong.zhang@uncc.edu

two samples that might otherwise appear to be indistinguishable if they were subjected only to the conventional probes, such as Raman spectroscopy, PL, XRD, and device characterization.

Additional or complementary information can be obtained by further applying "high-temperature" (HT) Raman spectroscopy. By high temperature, we mean that the temperature is high enough to induce some structural changes associated with the hidden structural or composition fluctuations. The combination of the two approaches or HPHT Raman spectroscopy, in conjunction with the "high spatial resolution" of the confocal diffraction limit detection, we have a very powerful "3H" laser spectroscopy approach for probing the structural variation and inhomogeneity, particularly in a complex alloy like $Cu_2ZnSnSe_4$ (CZTSe), with much greater sensitivity and efficiency.

The emerging photovoltaic material CZTSe may be grown by various techniques, but none of them has yet been able to achieve an efficiency close to the Shockley-Quisser limit [5]. This approach offers another useful tool for assessing the potential of an individual technology path by providing an efficient way to distinguish the materials that are otherwise indistinguishable when the conventional characterization tools are applied. It can also provide complementary information for the more direct structural or elemental characterization techniques, such as TEM [6] and atom probe tomography [7].

II. EXPERIMENTAL DETAILS

All Raman measurements are performed with a Horiba Jobin Yvon HR800 confocal Raman system using a 532-nm laser. The spectral dispersion is 0.44 cm^{-1}/pixel with a 1200-g/mm grating. The room-temperature measurement is carried out with a 100x objective lens with a numerical aperture NA = 0.9. The diffraction limit laser spot size is 0.76 μm, and the spatial resolution of the measurement is about half the laser spot size. A 50x long working-distance lens with NA = 0.5 is used in the HT Raman measurements. The laser power is adjusted by either using neutral density filters or charging laser current. For the HT measurement, the samples are heated by a Linkam TS1500 heating system with temperature control accuracy of 1 °C. The HP-illuminated site is examined by scanning-electron-microscopy (SEM) as well as energy-dispersive–x-ray–spectroscopy (EDS) elementary analysis.

Three different CZTSe samples are measured: bare CZTSe film CZTSe_97 (*S*1), bare CZTSe film M3599_12 (*S*2), and a CZTSe solar-cell device M3602_21 (*S*3). For *S*1, the CZTSe film is prepared by selenizing the metal stacks composed of 300-nm Mo, 130-nm Zn, 155-nm Cu, and 180-nm Sn sputtered on an Asahi PV 200 glass substrate. The film compositions are $[Zn]/[Sn] \cong 1.25$ and $[Cu]/([Zn]+[Sn]) \cong 0.85$ in kesterite phase. The film is slightly thicker than 1 μm. A device with a nominally similar absorber is measured with approximately 5% efficiency. The *S*2 and *S*3 films are grown in vacuum with a coevaporation method on a soda-lime glass substrate, with 1-μm sputtered Mo back contact and a 150-Å *e*-beam-evaporated NaF precursor. The film thickness is 1.49 μm with $[Zn]/[Sn] \cong 1.32$ and $[Cu]/([Zn]+[Sn]) \cong 0.82$ for *S*2, and 1.3 μm with $[Zn]/[Sn] \cong 1.28$ and $[Cu]/([Zn]+[Sn]) \cong 0.87$ for *S*3. The device sample *S*3 is finished with a chemical-bath-deposited CdS layer, a sputtered resistive-conductive ZnO bilayer, *e*-beam-evaporated Ni/Al grids, and a MgF_2 anti-reflective coating. Details of the film growth and device processing can be found in Refs. [8,9]. A device with a nominally same absorber as *S*2 has an energy-conversion efficiency of approximately 8%, and the efficiency of *S*3 is also approximately 8%.

III. RESULTS AND DISCUSSION

A. High-power Raman studies at room temperature

1. High-power effects at individual locations

In Fig. 1, Raman spectra of *S*1 and *S*2 are obtained with two powers, 32.8 μW (7.9×10^3 W/cm^2) and 146 μW (3.5×10^4 W/cm^2), from the same location with no grating movement between the two measurements. For

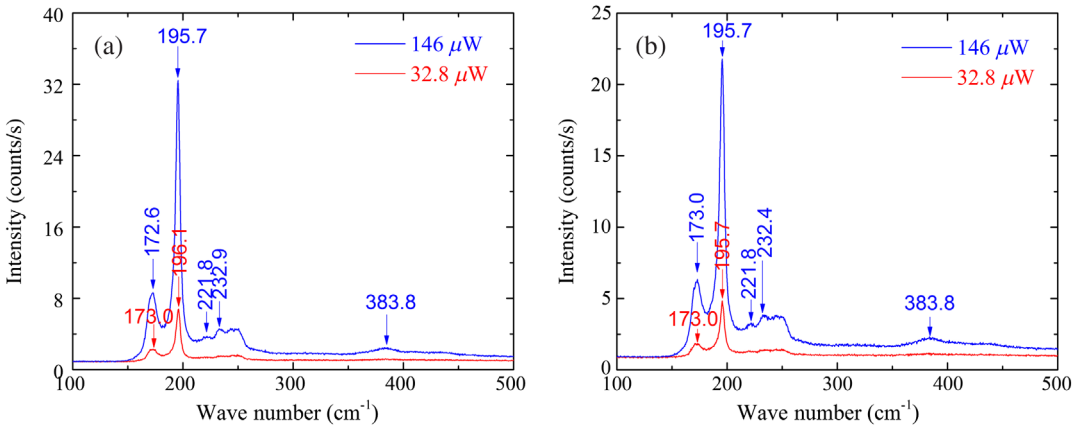

FIG. 1. Raman spectra of the bare CZTSe films measured at 32.8 and 146 μW: (a) *S*1, (b) *S*2.

*S*1, the primary CZTSe main Raman modes (196.1 and 173.0 cm^{-1}) experience a 0.4-cm^{-1} redshift when the laser power is increased from 32.8 to 146 μW. The observed redshift is reversible or the change is elastic when remeasured with the lower power. However, for *S*2, no shift is observed with the power change. The slight CZTSe Raman mode redshifts indicate that a small heating effect is introduced for the sputtered sample under 146-μW illumination, but the power level is not high enough to cause irreversible material modification. The comparison suggests some subtle structural difference between the two samples manifested in the difference in thermal conductivity. Despite the small heating effect found in *S*1, we will still consider 146 μW as a LP excitation level. Note that within each sample, the absolute position of the Raman mode may vary up to about 0.5 cm^{-1} due to sample inhomogeneity.

Figure 2 examines the effects of HP illumination by comparing the LP Raman spectra from the same location at 0.146 mW before and after 100-s illumination at 2.47 mW (5.9×10^5 W/cm^2) and a further 36 s at 4.5 mW (1.1×10^6 W/cm^2). After the 2.47-mW illumination, the illuminated spot shows some color change under optical microscope but no apparent ablation. However, the 4.5-mW illumination typically results in some local material ablation. We note that for a bulk Si even illuminated with the

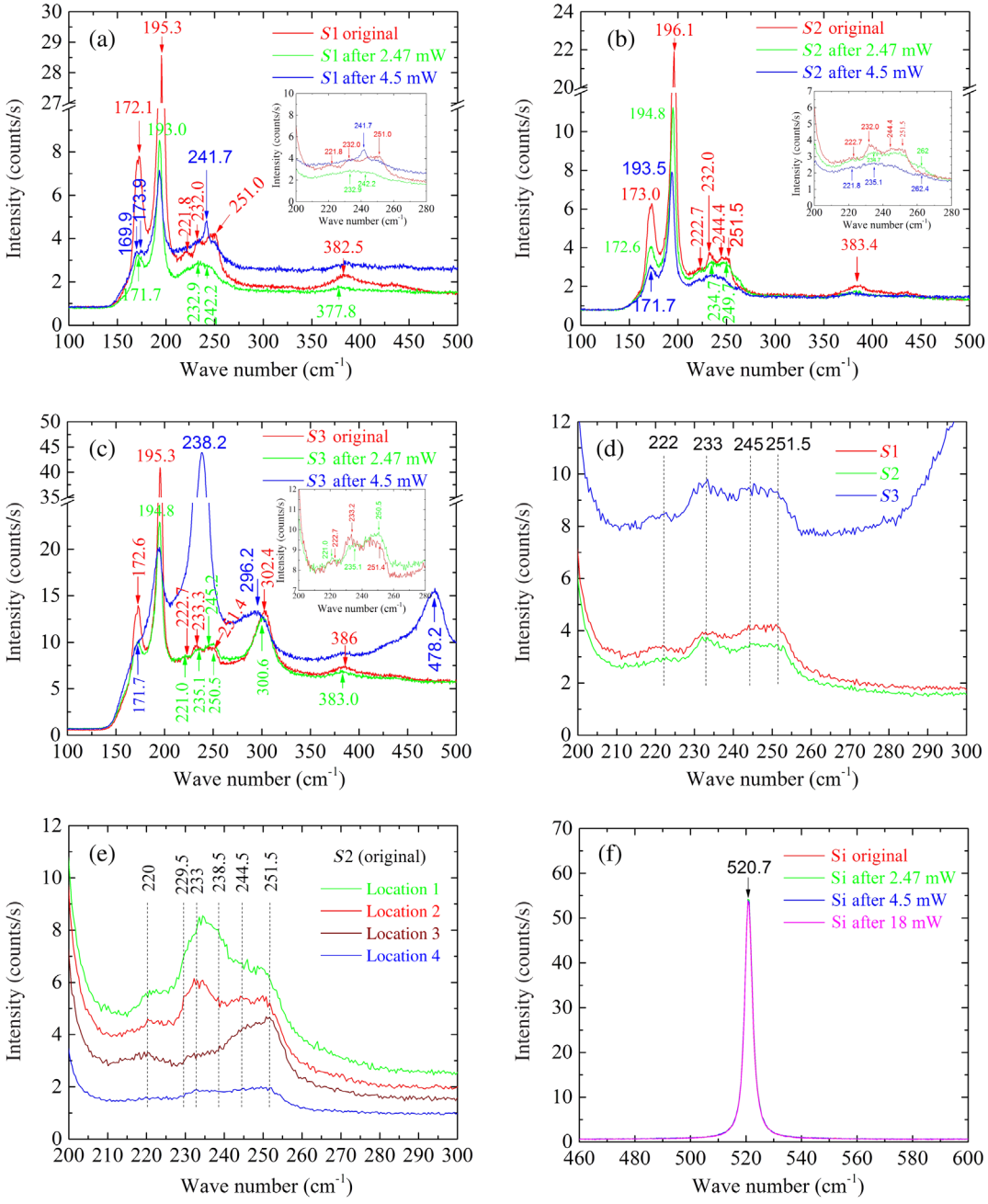

FIG. 2. Raman spectra of CZTSe and Si samples at 0.146 mW before and after being illuminated by high powers. (a) *S*1, (b) *S*2, (c) *S*3, (d) comparison of *S*1, *S*2, and *S*3, (e) comparison of different locations of *S*2, and (f) Si.

full power (approximately 20 mW, 4.9×10^6 W/cm^2), there is practically no change when returned to the LP condition.

The red curves in Figs. 2(a)–2(c) are typical Raman spectra from the three CZTSe samples measured first at 0.146 mW, and the green and blue curves are the corresponding spectra remeasured after the two higher-power illuminations. In their initial states, all three samples, in fact, exhibit rather similar Raman features: two intense Raman peaks at 195–196 and 172–173 cm^{-1} and a weak peak at 232–233 cm^{-1}, which are very close to the Raman peaks at 196, 173, and 231 cm^{-1} reported for a single-crystal CZTSe [10]. Additional weak peaks appear at approximately 222 cm^{-1}, 245 cm^{-1}, and 251.5 cm^{-1}. In Fig. 2(d), the spectral region of the multiple weak peaks ["mesalike" band to the right of the (195–196)-cm^{-1} peak] is compared directly among the three samples in their initial states, indicating that there is no significant or distinct difference between the samples prepared differently. As a matter of fact, more variations can be found within one sample, as shown in Fig. 2(e) comparing multiple locations of *S*2, due to composition inhomogeneity [11]. Therefore, it is impractical to use conventional Raman spectroscopy to reliably reveal potential structural variations from sample to sample. The peak of approximately 222 cm^{-1} is believed to be a transverse-optical (TO) Raman mode in *E* symmetry from kesterite structure based on theoretical calculations [12–14]. The peak of approximately 245 cm^{-1} was also reported to be CZTSe related in both experimental and theoretical studies [15–17]. The peak of approximately 251.5 cm^{-1} is close to the Raman modes of these possible secondary phases: 253 cm^{-1} of ZnSe [18–20], 251 cm^{-1} of Cu_2SnSe_3 [10], and approximately 250 cm^{-1} of amorphous selenium (*a*-Se) [21]. It is possible that extra selenium is present in CZTSe films, since they are fabricated in a Se-rich condition. *a*-Se may also have a weak feature at approximately 235 cm^{-1} due to the presence of crystalline-phase trigonal Se (*t*-Se) [21]. The Raman line near 303.6 cm^{-1} from the finished device *S*3 is known to be from CdS [22], which is the window layer of the CZTSe solar device. The origin of the broad band ranging from 380 to 390 cm^{-1} is unclear but common to the three samples. It could be the second-order feature of the 196 cm^{-1} mode. The purpose of this study is not to determine the exact origins of all these Raman features using Raman spectroscopy alone but to demonstrate a methodology that can offer more information than the conventional Raman probe. Such information may contribute to the ultimate understanding of such a complex material system when the results are correlated with those from other probing techniques.

A previous report indicated that the Raman spectra of a CZTSe sample showed no change in peak position and line shape with varying laser power up to 2.5 mW under 1-μm spot size [23]. However, it was reported that a CZTS sample under a comparable excitation density exhibited a very large shift (approximately 10 cm^{-1}) of the main Raman peak, resulting primarily from the order-to-disorder transition of the cation sublattice [24]. In this work, we find that even at 2.47 mW, significant changes already occur in CZTSe, not only at the illumination site but also in the region adjacent to that, and more interesting, the changes are sample dependent. At 4.5 mW, more drastic and sample-dependent changes occur both at the illumination site and in the adjacent region. Here, we focus on the changes at the illumination site, and we discuss the changes of the adjacent region later when discussing the Raman mapping data.

After the 2.47-mW illumination, as shown by the spectra in Figs. 2(a)–2(c) (in green), the two main CZTSe peaks at 195–196 and 171–172 cm^{-1} experience not only intensity reduction but also redshift in all three samples. For example, in *S*1, the CZTSe main peak at 195.3 cm^{-1} shifts to 193.0 cm^{-1} and 172.1 cm^{-1} to 171.7 cm^{-1}. The redshift of the $195-196$ cm^{-1} is the largest for *S*1, 2.3 cm^{-1}, compared to 1.3 cm^{-1} for *S*2, and 0.5 cm^{-1} for *S*3. These changes seem to suggest that the atomic bonds at the illuminated site are thermally expanded irreversibly as a result of the local heating if no atomic rearrangement occurs. However, it is possible that the redshift is caused by the cation sublattice disordering, as suggested for CZTS [24], although the magnitude in CZTSe is much smaller, despite the higher excitation density in our case, and sample dependent. The exact mechanism remains to be examined by a direct structural probe (e.g., TEM) but likely not as simple as the proposed disordering effect. The weak features in the mesalike band appear to smear out and weaken in both *S*1 and *S*2, as shown in Figs. 2(a) and 2(b). In *S*2, a new feature at approximately 262 cm^{-1} also emerges, whereas in *S*3, those weak features remain, but their relative intensities change, for instance, the peaks at approximately 235 and 250.5 cm^{-1} become more apparent, as shown in Fig. 2(c).

After illuminating further at 4.5 mW, with the spectra given in Figs. 2(a)–2(c) (in blue), the intensity of the strongest CZTSe peak initially at 195–196 cm^{-1} decreases further for all three samples, but the peak position remains nearly the same as that after the first HP illumination, except for *S*2, it shifts further from 194.8 to 193.5 cm^{-1}, resulting in the largest redshift of 2.6 cm^{-1} among all. For *S*1, as shown in Fig. 2(a), the intensity of the 193-cm^{-1} peak is reduced to only 17% of its original value before any high-power illumination, and the 172-cm^{-1} mode becomes a weak shoulder from 168 to 178 cm^{-1}. Interestingly, for *S*2, the main CZTSe peak intensity decreases only by a factor of 4, and the CZTSe peak of approximately 172 cm^{-1} remains sharp. For the spectral region of the mesalike band, a sharp peak emerges at 241.7 cm^{-1} as the

most prominent feature in *S*1 but not in *S*2 and S3. No significant further change in *S*2 except that the feature of approximately 262 cm^{-1} is slightly better resolved. In *S*3, one very strong sharp peak at 238.2 cm^{-1} appears, which is accompanied by a second-order peak at 478.2 cm^{-1} (and a third-order peak at approximately 714 cm^{-1}, not shown) and a broad band at approximately 296 cm^{-1}. Obviously, the second HP illumination brings more qualitatively different changes to these samples. The contrast between *S*1 and *S*2 suggests that the CZTSe structure prepared by coevaporation seems to be more robust than that prepared by sputtering against HP-illumination-induced structural modifications.

Regarding the newly appearing peak of approximately 242 cm^{-1} in *S*1, although it was previously reported as a CZTSe Raman mode [25,26], it actually matches the A_{1g} Raman mode of $MoSe_2$ [27]. Since it appears only after the second HP illumination, at least it cannot be intrinsic to CZTSe. When *S*1 is examined from the cleaved edge under LP, $MoSe_2$ is found to be the main component at the substrate-film boundary and reduces gradually but exists at least in most parts of the CZTSe film, suggesting significant Mo interdiffusion during fabrication [28]. The weak peak of approximately 262 cm^{-1} in *S*2 turns out to be the Se-Se stretching mode of Se_2 ions in Cu_xSe_y [29–32] coming from the periphery of the illuminated spot, which is apparent in the surface Raman mapping result that we discuss later. The peak of approximately 238 cm^{-1} in *S*3 is most likely the A_1 mode of *t*-Se [21,33]. It was shown that as a result of photocrystallization, a broad band at approximately 250 cm^{-1} and a shoulder at approximately 235 cm^{-1} observed in an *a*-Se film became two resolved peaks: *E*-symmetry mode at 233 cm^{-1} and A_1-symmetry mode at 237 cm^{-1} of *t*-Se [21]. This transformation matches our observations in *S*3 before and after the second HP illumination, which suggests the possibility that *a*-Se exists in the as-deposited CZTSe film, and after the second HP illumination, *a*-Se is nearly completely crystallized to *t*-Se since no 250-cm^{-1} peak remains. One may notice that the intensity of the *a*-Se mode at approximately 250 cm^{-1} initially observed in the as-grown CZTSe film is much lower than the intensity of approximately 238 cm^{-1} that appears after the second HP illumination. It is possible that the partial decomposition of CZTSe provides more selenium, which contributes to the strong *t*-Se Raman mode. Similar changes caused by HP illumination are also observed from other similar coevaporated CZTSe devices. Table I summarizes the Raman modes before and after the first and second HP illumination.

In summary, changes in Raman spectra from all three CZTSe samples after HP illumination indicate partial decomposition and plastic changes of the materials. However, different samples respond rather differently to HP illumination, indicating that seemingly similar CZTSe materials may differ significantly in their microscopic structures. As a comparison to a conventional semiconductor, Fig. 2(f) gives Raman spectra collected from a Si sample before and after HP illumination. Illuminated with different laser powers up to a maximum of 18.9 mW (4.5×10^6 W/cm^2) for 50 to 400 s, the Si Raman spectra look almost the same as their original spectrum collected with 0.149 mW. It was also found previously that the highest power was, in general, safe for an epitaxial GaAs sample but could induce a structure change when a dislocation-type defect was illuminated [34]. Apparently, quaternary CZTSe is structurally not as robust as an elemental or binary semiconductor such as Si and GaAs. The contrast is mostly because of the difference in chemical bonding strength but may be also the structural defects and lower thermal conductivity of the polycrystalline film.

TABLE I. Summary of Raman modes from three CZTSe samples before and after high-power illumination.

Sample	Before	After first illumination	After second illumination	Origin
*S*1	172.1 cm^{-1}	171.7 cm^{-1}	169.9 cm^{-1}	CZTSe
	195.3 cm^{-1}	193.0 cm^{-1}	193.0 cm^{-1}	CZTSe
	222 cm^{-1}			CZTSe
	233 cm^{-1}			CZTSe
	245 cm^{-1}			CZTSe
	251.5 cm^{-1}			*a*-Se
			241.7 cm^{-1}	$MoSe_2$
*S*2	173.0 cm^{-1}	172.6 cm^{-1}	171.7 cm^{-1}	CZTSe
	196.1 cm^{-1}	194.8 cm^{-1}	193.5 cm^{-1}	CZTSe
	222 cm^{-1}			CZTSe
	233 cm^{-1}			CZTSe
	245 cm^{-1}			CZTSe
	251.5 cm^{-1}			*a*-Se
		262 cm^{-1}	262.4 cm^{-1}	Cu_xSe_y
*S*3	172.6 cm^{-1}	171.7 cm^{-1}	~172 cm^{-1}	CZTSe
	195.3 cm^{-1}	194.8 cm^{-1}	194.8 cm^{-1}	CZTSe
	222 cm^{-1}	222 cm^{-1}		CZTSe
	233 cm^{-1}	233 cm^{-1}		CZTSe
	245 cm^{-1}	245 cm^{-1}		CZTSe
	251.1 cm^{-1}	250.5 cm^{-1}		*a*-Se
		235.1 cm^{-1}	238.2 cm^{-1}	*t*-Se
			478.2 cm^{-1}, 714 cm^{-1}	*t*-Se
	302.4 cm^{-1}	300.6 cm^{-1}	296.2 cm^{-1}	CdS

2. Raman mapping near the illuminated site

Two-dimensional Raman mapping is performed to examine the spatial extension of the local heating effect caused by HP illumination on the CZTSe samples, as shown in Fig. 3 for 2.47-mW illumination. One random spot from each sample surface is first illuminated by

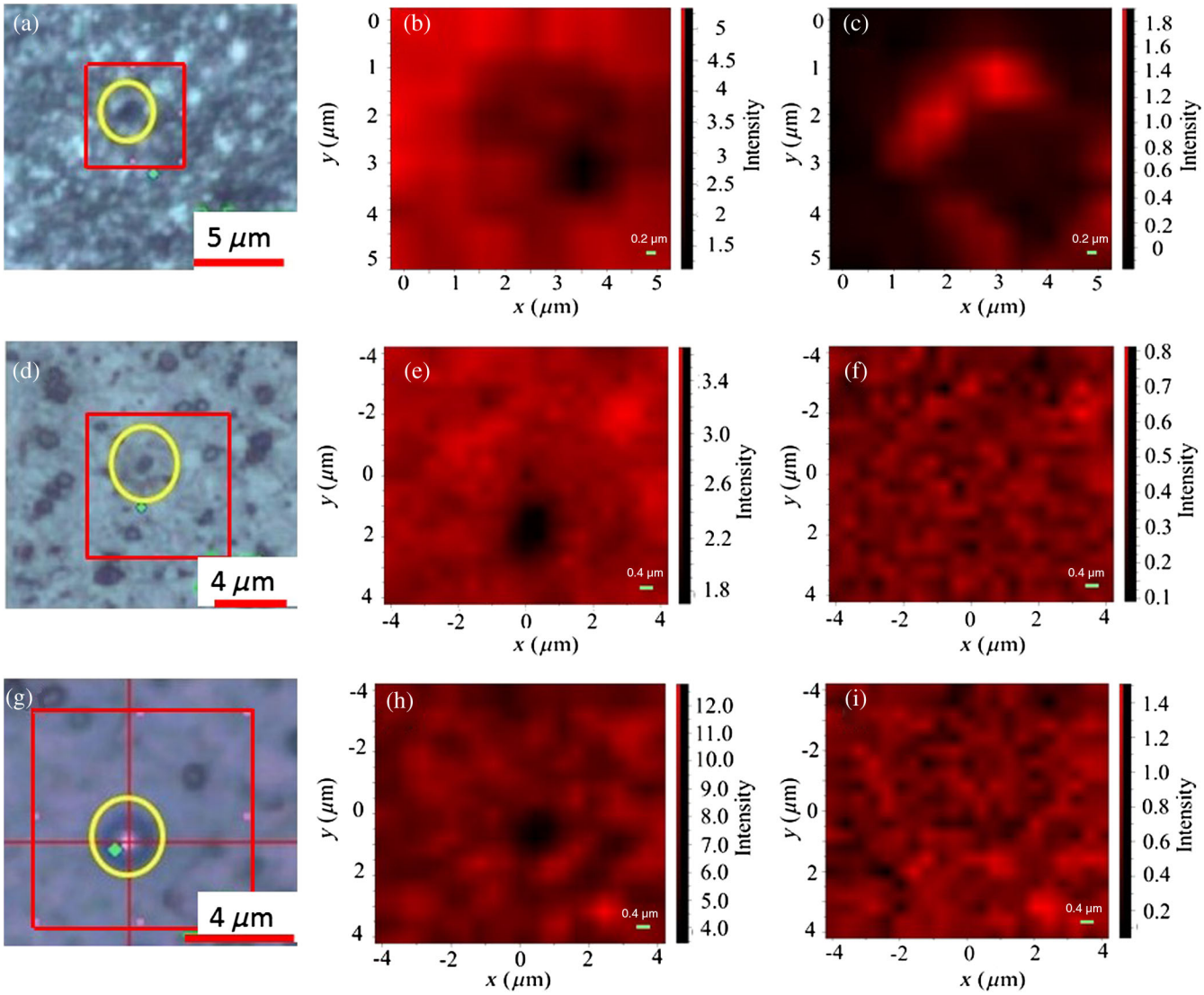

FIG. 3. $S1$, $S2$, and $S3$ Raman mapping after one spot being illuminated by 2.47 mW for 100 s: (a), (d), and (g) optical images of the illuminated spot (the red square indicates the area of Raman mapping); (b), (e), and (h) Raman mapping of the primary CZTSe mode at 196 cm^{-1}; (c), (f), and (i) Raman mapping of the Cu_xSe_y mode at 261 cm^{-1}.

2.47 mW for 100 s. Raman mapping is then acquired with 0.146-mW laser power for a 5×5 μm^2 or 8×8 μm^2 area centered at the illuminated spot. For all three samples, the illuminated spot appears darker after being illuminated, as shown in the optical images of Figs. 3(a), 3(d), and 3(g). For each sample, Raman intensity mapping reveals a dark circle for the 196-cm^{-1} peak, as shown in Figs. 3(b), 3(e), and 3(h), confirming the intensity reduction of this mode shown in Fig. 2. In the Raman mapping of $S1$, a Raman peak at approximately 261 cm^{-1} is observed in a ring outside of the illumination site, as evident in Fig. 3(c). However, in the mapping results of $S2$ and $S3$, the 261 cm^{-1} peak is not observed, and the intensity maps of $220 - 270$ cm^{-1} show no significant spatial variation, as shown in Figs. 3(f) and 3(i). The appearance of a peak of approximately 261 cm^{-1} suggests the formation of Cu_xSe_y [24–27] occurring mostly at some distance away from the illumination site, which likely results from a specific temperature profile caused by the laser heating. The formation of the ring structure also explains why when measured at the illumination site, the Cu_xSe_y feature is not resolved in $S1$ and $S3$, and only very weak in $S2$, as shown in Fig. 2(b). In Fig. 4(a), for $S1$, a comparison is given between the spectra measured at the illumination site and a typical spot on the Cu_xSe_y ring. Clearly, a sharp 261.1-cm^{-1} peak appears from the Cu_xSe_y ring but not at the illumination site. Additionally, on the Cu_xSe_y ring, the CZTSe modes 195.7 and 171.7 cm^{-1} show no significant shift, and their intensities are much stronger than those of the illumination site but still only about half of the values before the illumination. The findings indicate that the HP illumination might lead to partial CZTSe decomposition on

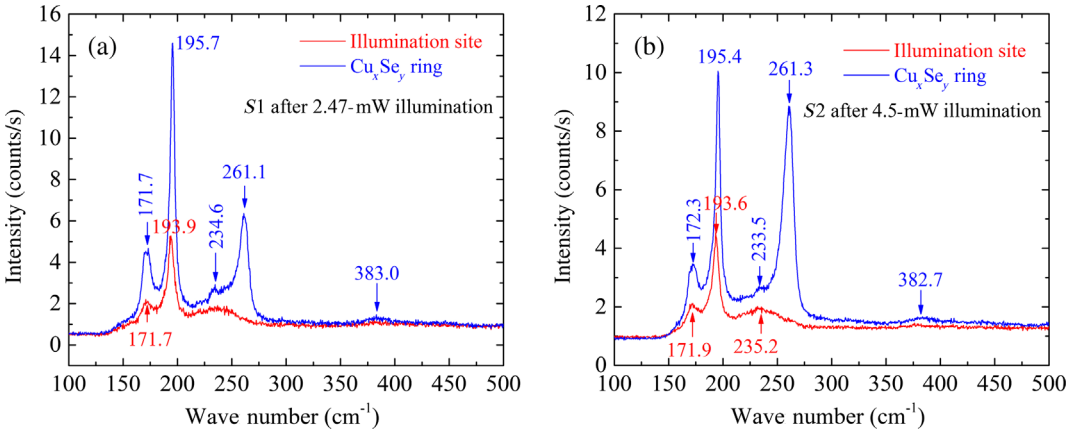

FIG. 4. Comparison of Raman spectra measured at the illumination site and Cu_xSe_y ring: (a) $S1$ after 2.47-mW illumination; (b) $S2$ after 4.5-mW illumination.

the Cu_xSe_y ring, though not as much as at the illumination site.

The Raman mapping of the primary CZTSe mode at 196 cm^{-1} reveals most directly the spatial extension the material being affected by the local heating. For $S1$, as shown in Fig. 3(a), beyond the darkest 1-μm circle (comparable to the laser spot size of approximately 0.76 μm) at the illumination site, a dark area with a diameter of approximately 3 μm comparable to the size of the 261 cm^{-1} Cu_xSe_y ring is observed. On the other hand, the illumination affects only an area of approximately 1.5 μm diameter in $S2$ and less than 1 μm diameter in $S3$. The difference between $S1$ and $S2$ seems to suggest that the two nominally similar films have rather different thermal conductivities, which might be partially responsible for the different responses in the structural change that we mention above. The extra layers above CZTSe in device $S3$ might improve the thermal conductivity of the structure as a whole, thus, showing the least spatial extension. The contrast between $S1$ and $S2$ suggests that the CZTSe absorber layer prepared by the sputtering method is more sensitive to HP illumination than the film fabricated by the coevaporation method.

Figure 5 shows the mapping results with 0.146 mW after 4.5-mW illumination. Compared to the results of 2.47-mW illumination, larger affected regions are revealed in the optical images in Figs. 5(a), 5(d), and 5(g). Raman mapping in Fig. 5(b) shows that the 196-cm^{-1} peak intensity of $S1$ reduces in a circular region with a diameter larger than 6 μm. The affected area of $S2$ in Fig. 5(e) also enlarges to about 5 μm in diameter. For $S3$, the affected area in Fig. 5(h) has a diameter only about 2 μm. The extra layers in the CZTSe device again offer some protection to the CZTSe absorber. In the intensity map of the 261-cm^{-1} peak, a Cu_xSe_y-rich ring still exists in $S1$ as shown in Fig. 5(c), but now a similar Cu_xSe_y ring also appears in $S2$, although smaller, as shown in Fig. 5(f). Figure 4(b) compares the representative spectra measured at the ring and the illuminated site for $S2$. Similar to $S1$, a strong Cu_xSe_y Raman peak is observed only from the ring, and the CZTSe main peak shows a higher peak intensity and smaller redshift compared to the illumination site. The size of the Cu_xSe_y-rich ring reflects the size of the heated region that reaches the optimal phase-transition temperature, which is comparable to the affected CZTSe area in $S1$ but smaller in $S2$. For $S3$, again, no Cu_xSe_y ring is observed. However, consistent with the observation of a strong Raman peak at approximately 238 cm^{-1} shown in Fig. 2(c) due to the formation of t-Se at the illuminated site under the same HP illumination, the Raman map of 238 cm^{-1}, Fig. 5(i), shows a bright region with a comparable size of the dark region for the CZTSe mode in Fig. 5(h). The affected CZTSe area and the size of the Cu_xSe_y ring both depend on the thermal conductivity of the material which differs significantly between the three samples.

It has been shown through TEM and other elemental studies that polycrystalline CZTSe films tend to exhibit various sizes of voids, domains of the secondary phases, and elemental segregation at the domain or interface boundaries, and these defects depend sensitively on the growth and postgrowth treatment conditions [6,7,35]. It is well known that grain boundaries and defects can have major impact on the thermal conductivity, which, in turn, can significantly affect the size and shape of a new microstructure generated by local laser-heating-induced structural modification [36]. The structural modifications that we observe in the vicinity of the illuminated site clearly indicate that $S1$ has a lower thermal conductivity than $S2$ and $S3$, implying that the film produced by sputtering is likely more defective. Furthermore, all these samples are likely to have a-Se as grown, and the sputtered sample has more interdiffused Mo in the film, which is supported by the cleaved-edge Raman probe [28] and is further confirmed by EDS analysis that we give later.

While it is generally known that structural imperfections such as dislocations and grain boundaries reduce material thermal conductivity [37], the substrate may also affect the thermal conductivity of a thin film [38]. In these CZTSe films, the Mo layer and glass substrate can, in principle, improve heat dissipation of the laser-induced heating,

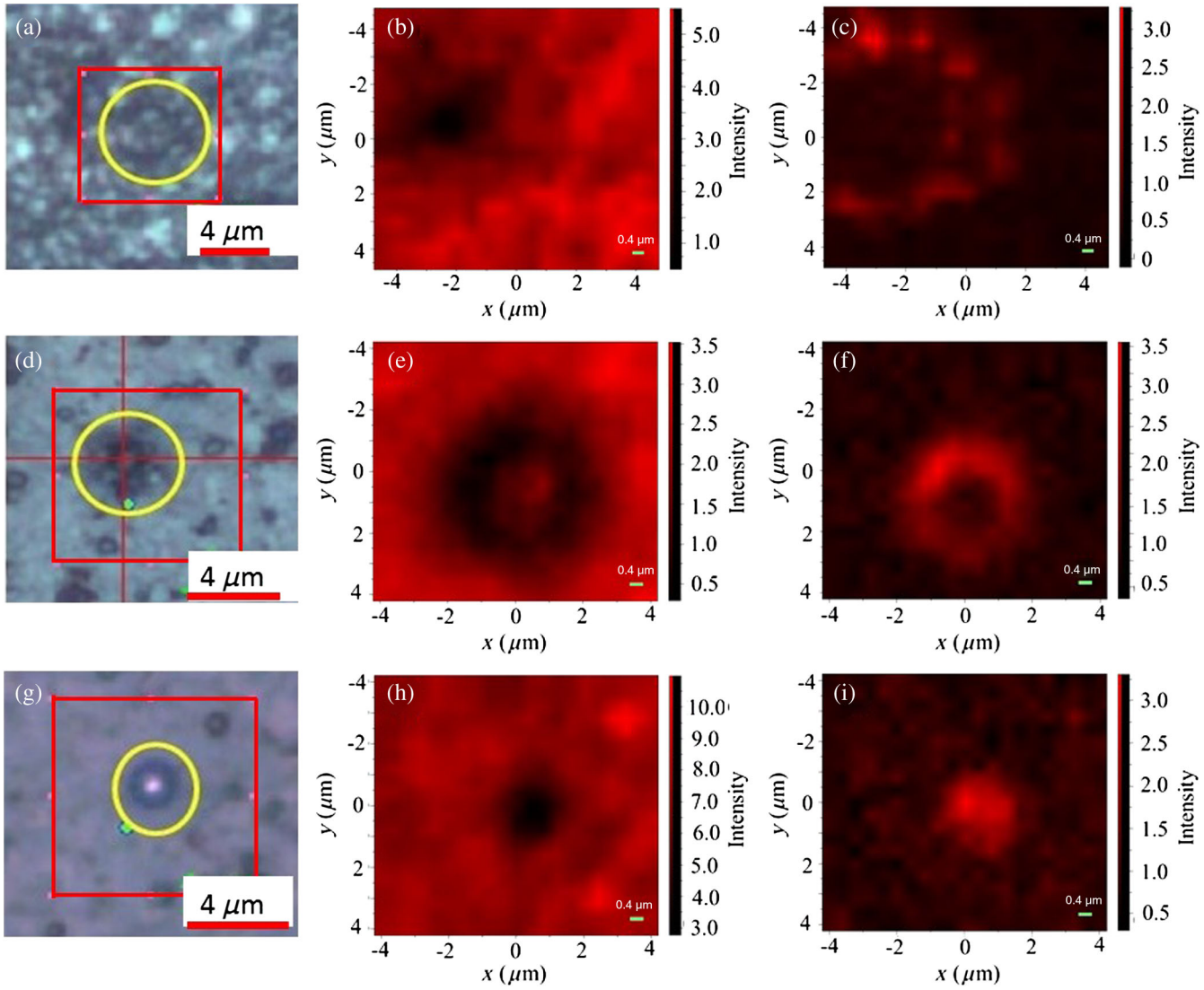

FIG. 5. *S*1, *S*2, and *S*3 Raman mapping after one spot being illuminated by 4.5 mW for 36 s: (a), (d), and (g) optical images of the illuminated spot (the red square indicates the area of Raman mapping); (b), (e), and (h) Raman mapping of the primary CZTSe mode at 196 cm^{-1}; (c) and (f) Raman mapping of the Cu_xSe_y mode at 261 cm^{-1}; (i) Raman mapping of the *t*-Se mode at 238 cm^{-1}.

which yields a higher effective thermal conductivity. However, because of the low thermal conductivity of CZTSe [39] and short absorption length below the film thickness, the effect of the underneath layers is expected to be less significant. In fact, if it were significant, one would find the thermal conductivity being the highest in *S*1, which is apparently contrary to the experimental findings. Therefore, the lower crystallinity of *S*1 is likely the primary reason for its low thermal conductivity. In addition to revealing the microscopic scale structural differences between samples, the HP illumination provides a way to generate new microscopic structures on an as-grown material for various possible applications, such as Cu_xSe_y rings in samples like *S*1 and *S*2, and *t*-Se disks in samples like *S*3. A similar method was used to generate graphene disks on an epitaxially deposited SiC [36].

B. High-temperature studies

High temperature is often used for material thermal annealing. A few recent studies of CZT(S,Se) have shown that the Cu and Zn distribution in the cation sublattice can be modified through thermal annealing with order-to-disorder transition temperature being $T_c \sim 260\,°C$ for CZTS and approximately 200 °C for CZTSe [40–42]. There are significant differences between the annealing study and high-temperature study performed in this work both in terms of technique and purpose. The former typically requires a very long annealing time (e.g., 24 h) at a set temperature for the atomic migration between different lattice sites to reach an equilibrium distribution. In our case, the sample stays only at each temperature step for a few minutes, long enough to reach a stable temperature but ideally not to induce interlattice-site atomic migration,

although the migration might still occur for some out-of-place atoms, such as interstitials atoms.

High-temperature Raman spectra of a random spot from each sample are collected with a step of 20 or 40 °C starting from room temperature up to about 900 °C using 0.147-mW laser power with a 50x long working-distance lens. Raman spectra at representative temperatures are shown in Fig. 6. For *S*1, as in Fig. 6(a), the main CZTSe peak at approximately 196 cm^{-1} starts redshifting when the temperature is raised to above 60 °C, at a rate about

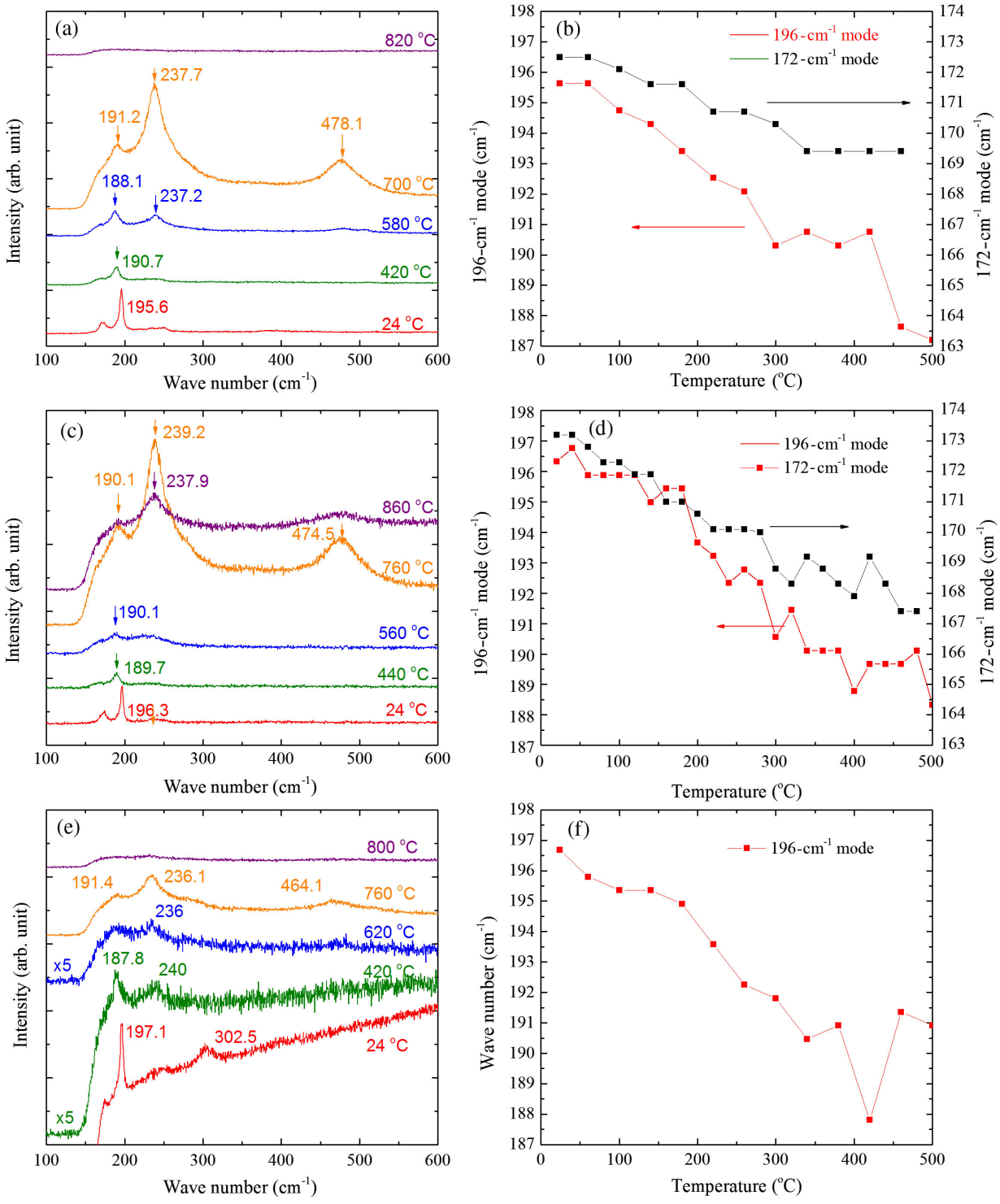

FIG. 6. High-temperature study of three samples. (a), (c), and (e) Raman spectra at different temperatures; (b), (d), and (f) peak positions of CZTSe Raman modes at different temperatures.

0.0174 ± 0.0013 cm^{-1}/°C, which is obtained from the linear fit in Fig. 6(b). As indicated in Fig. 1, at this power level, a small heating is expected for this sample. The residual laser heating can explain why no shift is observed when the sample temperature is below 60 °C, as shown in Fig. 6(b). Using the obtained rate, we can estimate the laser-induced local heating in $S1$ (see Fig. 1) at 0.147 mW to be around 23 °C with respect to room temperature. Another CZTSe Raman mode at 172 cm^{-1} also redshifts with raising temperature but exhibiting a smaller rate than the 196-cm^{-1} peak, as shown in Fig. 6(b). It shows small intensity change until reaching around 200 °C. At higher temperatures, it starts to show significant intensity reduction and peak broadening and finally becomes a weak shoulder in the spectrum at 420 °C. With increasing temperature, the mesalike band from 220 to 250 cm^{-1} becomes narrower and evolves into a well-defined strong peak at approximately 237 cm^{-1} at 580 °C, together with the appearance of its second-order mode at approximately 478 cm^{-1}. These two peaks reach their maximum intensities at around 700 °C and gradually diminish after that. As described in the S3 HP study, the strong peaks at approximately 238 cm^{-1} and approximately 478 cm^{-1} are t-Se modes [21]. The main CZTSe peak reaches the largest redshift at around 500 °C. With further increased temperature, when the 237-cm^{-1} peak starts to emerge, the 196-cm^{-1} peak begins to blueshift instead. We note that the Raman peak of approximately 188 cm^{-1} observed at a temperature above 500 °C is likely not the CZTSe peak anymore but from a secondary-phase Cu_2SnSe_3 or ZnSe. On a separated test where the sample is brought up only to 480 °C, upon returning to room temperature, the primary CZTSe Raman peak is not observable except at some isolated locations, indicating that CZTSe is mostly decomposed above 500 °C.

The results for $S2$ are shown in Fig. 6(c) with typical Raman spectra at selected temperatures and Fig. 6(d) for the peak positions of the 196- and 172-cm^{-1} modes with varying temperature. Similar to $S1$, t-Se gradually becomes the dominant component when the temperature is higher than 600 °C, reaching its maximum intensity at around 700 °C. The similar heating results for $S3$ are shown in Figs. 6(e) and 6(f). The t-Se modes are very weak between 380 and 660 °C and become clear and dominant when the temperature is above 700 °C and disappears at around 800 °C.

Another piece of $S3$ is also tested with the temperature increased only to 400 °C and then cooled down to room temperature. For the most part, the absorber layer is found to recover at least 60% of the original intensity for the CZTSe main peak of approximately 196 cm^{-1}, although the frequency redshifts significantly to 192.6 cm^{-1}, but the CdS mode at approximately 303 cm^{-1} can hardly be observed, indicating that the CdS window layer is decomposed. The shift of the primary CZTSe Raman mode can be explained as due to some degree of thermal-induced disordering in the cation sublattice [41], since 400 °C is substantially above the critical temperature. Some dark spots surrounded with bright halo are observed. An example is shown in Fig. 7 where four Raman spectra obtained at different distances from one such black spot with an optical image in the inset. At the center of the dark spot, resonant t-Se Raman modes are observed at 241, 482, and 717 cm^{-1} together with a shifted CZTSe peak at 192.6 cm^{-1}. The farther away from the black spot center, the smaller the Se Raman signals. These observations indicate that after the HT measurement, the dark spot becomes rich in selenium, and the decomposition process at high temperature is not uniform across the film.

Although for $S1$ and $S2$, the t-Se modes of approximately 238 and 478 cm^{-1} are not observed in the HP study, these modes have now been observed from the HT study with uniform heating. We may conclude that the peaks of approximately 238 and 478 cm^{-1} in Fig. 2(c) for $S3$ after HP illumination do not originate from the extra layers of the CZTSe device, since the bare film samples do not have the extra layers beyond the absorber.

For the HT study, other than the fact that the t-Se peak seems to appear at a somewhat lower temperature in $S3$, the results of the uniform heating are qualitatively similar for all three samples. However, they differ significantly from the HP study. Perhaps t-Se can, in principle, also appear in $S1$ and $S2$ if they are illuminated by a higher laser power. However, it is impractical because the materials will be seriously ablated when a high power is used. It is likely the processes to make the absorber material a finished device cause the absorber layer in $S3$ to be more sensitive to HP

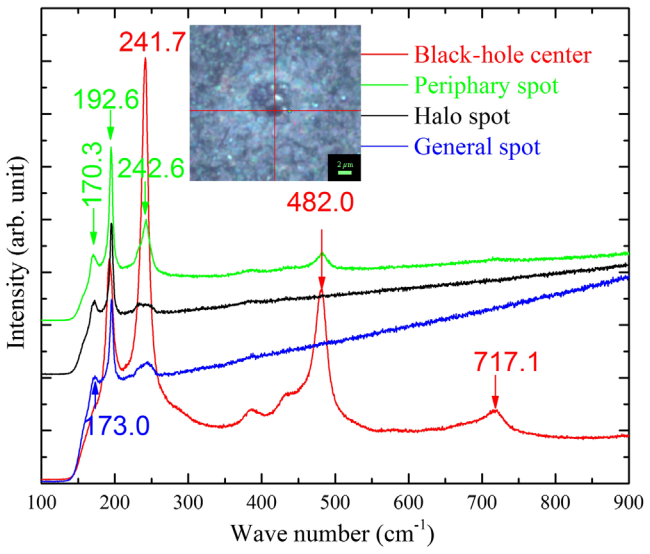

FIG. 7. Room temperature Raman spectra of $S3$ near a dark spot after high-temperature study. The inset shows an optical image of the area.

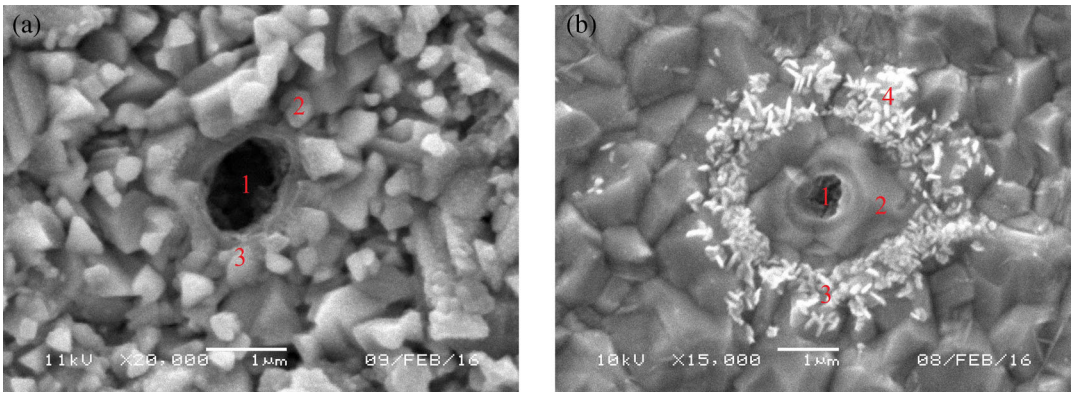

FIG. 8. SEM images of *S*1 and *S*2 surface spots being illuminated by 4.5 mW: (a) *S*1, (b) *S*2. The scale bars are 1 μm for both images.

and HT for the formation of *t*-Se. We also notice that the three orders of the *t*-Se Raman modes shown in Fig. 7 induced by uniform heating are systematically blueshifted from those in Fig. 2(c) by HP illumination, suggesting that they are in different states of strain, and, thus, the local and uniform heating are not equivalent.

Cu_xSe_y as a new phase is often observed after HP illumination. However, no Cu_xSe_y mode at 261 cm^{-1} is observed in the HT measurements from any of the three samples. In the high-temperature study, the entire sample is heated uniformly, whereas laser illumination generates highly localized uniform heating, thus, a highly nonuniform stress field. Thus, lateral thermal conductivity and stress both play a role in the formation of the Cu_xSe_y-rich ring.

Finally, the local temperature rise induced by HP illumination can be estimated by comparing the Raman frequency change of the main CZTSe Raman peak between the lower and high power spectrum, assuming the local heating effect is elastic. Based on the redshifts observed with the 2.47-mW illumination—4.9 cm^{-1} (*S*1), 3.6 cm^{-1} (*S*2), and 2.2 cm^{-1} (*S*3)—and the temperature dependences shown in Figs. 6(b), 6(d), and 6(f), we estimate that the local temperature reaches approximately 280 °C in *S*1, approximately 260 °C in *S*2, and approximately 200 °C in *S*3. The results of the higher-power 4.5-mW illumination are inappropriate for such estimate because the CZTSe material right at the illumination site is either ablated or converted into *t*-Se (see Fig. 5); thus, the measured CZTSe signal of much reduced intensity is partially from the adjacent area that might not be heated as much. Furthermore, HP illumination might induce inelastic local strain and/or change in the sublattice ordering, which can make the local heating effect more complicated than a simple temperature change. These potential effects can explain the differences for the *t*-Se–related peaks observed in the HP and HT measurements.

C. EDS after HP illumination

EDS is also performed to study the elemental compositions near the illuminated site after HP illumination. The SEM images of 4.5-mW illuminated sites from *S*1 and *S*2 are shown in Fig. 8, and the elemental ratios are summarized in Table II. After the HP illumination, the illuminated center of *S*1 shows a considerable amount of Mo and the highest Se concentration but the lowest Cu concentration, which is consistent with the formation of $MoSe_2$ at the illuminated site where part of the film is ablated in the HP study. In contrast, the *S*2 illuminated site shows the lowest Se and Cu concentration but the highest Zn and Sn concentration, indicating different structure changes after HP illumination in these two films. For both *S*1 and *S*2, the illuminated sites have very low $Cu/(Zn+Sn)$ ratios; however, the underlying changes are somewhat different.

TABLE II. EDS results of *S*1 and *S*2 after surface spots being illuminated by 4.5 mW. The numbers in the parentheses are the nominal values for the samples.

	Regions	Cu (%)	Zn (%)	Sn (%)	Se (%)	Zn/Sn	Cu/(Zn + Sn)	Mo (%)
*S*1	1	6.7	11.7	8.6	65.6	1.36	0.33	7.4
	2	17.5	16.9	11.1	54.5	1.52	0.67	0
	3	19.6	16.1	9.3	55.0	1.73	0.71	0
	General area	18.9	15.6	9.1	56.4	1.71 (1.25)	0.76 (0.85)	0
*S*2	1	16.3	31.0	19.1	33.6	1.62	0.32	0
	2	17.8	16.9	13.4	51.9	1.26	0.59	0
	3	22.9	11.8	9.9	55.4	1.19	1.05	0
	4	21.8	12.4	9.9	55.9	1.25	0.99	0
	General area	21.1	12.6	10.0	56.3	1.26 (1.32)	0.94 (0.82)	0

Away from the illuminated site, the bright ring in Fig. 8(b) for *S*2 exhibits higher Cu and Se concentrations as well as a higher $Cu/(Zn + Sn)$ ratio than the general area, which is consistent with the Raman mapping result that a Cu_xSe_y-rich ring surrounding the illuminated site appears after 4.5-mW illumination. However, the Raman mapping for *S*1, Fig. 5(b), also shows a Cu_xSe_y ring though less prominent, and the Cu_xSe_y-rich region does not appear bright in the SEM image of Fig. 8(a). Also, one can see that the laser-ablated area on *S*1 is much larger than that on *S*2, which again confirms the surface Raman mapping results in Fig. 5.

IV. SUMMARY AND CONCLUSIONS

In this work, by combining spatially resolved HP and HT Raman spectroscopy, we are able to reveal the significant differences in the microscopic structure of polycrystalline CZTSe films that will otherwise appear very similar using conventional characterization tools, such as Raman spectroscopy and XRD. The materials prepared by different methods are found to respond differently to local HP illumination in terms of the frequency changes of the CZTSe Raman modes, formation of secondary phases at and near the illumination site, and spatial extension in the impact. These differentiations are closely related to the differences in the thermal conductivity of the materials, which, in turn, reflects the different conditions of structural defects.

In general, the coevaporated films are structurally more robust than the sputtered film, although the threshold of laser-induced structural change is over 2 orders of magnitude lower for CZTSe than for Si. All materials seem to have *a*-Se, which upon heating by laser can form different secondary phases either at or near the illuminated site, depending on the sample.

Specifically, for the two bare CZTSe films, a Cu_xSe_y-rich ring enclosing the illuminated site is induced by HP illumination, but the size of the ring is found to be significantly larger for the sputtered sample than the coevaporated one. In the sputtered sample but not in the coevaporated one, HP illumination also forms $MoSe_2$ at the illumination site, suggesting more Mo interdiffusion in the former. Despite amorphous Se (*a*-Se) likely being present in all samples, only the CZTSe device shows the strong crystalline Se (*t*-Se) Raman modes of approximately 238, 478, and 714 cm^{-1} at the illumination site after HP illumination. EDS analyses confirm the spectroscopy conclusions.

On one hand, the HT Raman measurements reveal the different decomposition processes of the three different samples, and on the other hand, they further confirm that *t*-Se results from photocrystallization of *a*-Se or CZTSe decomposition. *a*-Se–to–*t*-Se transition most easily occurs in the device sample. The thermal decomposition of CZTSe occurs at about 480 °C in the N_2 environment.

The combination of high power and high temperature in the Raman study in conjunction with high spatial resolution (3H) can offer an effective approach to reveal the existence of the microscopic structural variations of complex alloys like CZTSe. This technique is likely most suitable and effective for a polycrystalline material with a relatively low thermal conductivity, which is usually the case for a complex semiconductor alloy. An appropriate laser power depending on the specific material of interest should be chosen such that it is high enough to induce a local structural change but without major material ablation. This spectroscopy method does not yield directly the structural information before the induced changes. Correlative studies with other direct structural characterization techniques are needed to derive more concrete understanding of the underlying atomic structures of the materials. In addition to a spectroscopy technique for revealing the microscopic scale structural differences between samples, the HP illumination provides a way to generate microscopic structures on an as-grown material with many potential applications in electronics and optoelectronics.

ACKNOWLEDGMENTS

We are very grateful to Dr. I. Repins (NREL) for providing the coevaporated samples and helpful discussions. Y. Z. acknowledges the support of Bissell Distinguished Professorship.

[1] D. A. Cremers and A. K. Knight, *Laser-Induced Breakdown Spectroscopy* (Wiley Online Library, New York, 2000).

[2] B. Gault, F. Vurpillot, A. Vella, M. Gilbert, A. Menand, D. Blavette, and B. Deconihout, Design of a femtosecond laser assisted tomographic atom probe, Rev. Sci. Instrum. **77**, 043705 (2006).

[3] F. Vurpillot, M. Gilbert, A. Vella, and B. Deconihout, Femtosecond laser atom probe tomography: Principles and applications, Microsc. Microanal. **13**, 1606 (2007).

[4] Q. Chen, H. Liu, H.-S. Kim, Y. Liu, M. Yang, N. Yue, G. Ren, K. Zhu, S. Liu, N.-G. Park, and Y. Zhang, Multiple-Stage Structure Transformation of Organic-Inorganic Hybrid Perovskite $CH_3NH_3PbI_3$, Phys. Rev. X **6**, 031042 (2016).

[5] W. Shockley and H. J. Queisser, Detailed balance limit of efficiency of *p-n* junction solar cells, J. Appl. Phys. **32**, 510 (1961).

[6] M. Buffiere, G. Brammertz, M. Batuk, C. Verbist, D. Mangin, C. Koble, J. Hadermann, M. Meuris, and J. Poortmans, Microstructural analysis of 9.7% efficient $Cu_2ZnSnSe_4$ thin film solar cells, Appl. Phys. Lett. **105**, 183903 (2014).

[7] T. Schwarz, O. Cojocaru-Mirédin, P. Choi, M. Mousel, A. Redinger, S. Siebentritt, and D. Raabe, Atom probe tomography study of internal interfaces in $Cu_2ZnSnSe_4$ thin-films, J. Appl. Phys. **118**, 095302 (2015).

[8] I. Repins, C. Beall, N. Vora, C. DeHart, D. Kuciauskas, P. Dippo, B. To, J. Mann, W.-C. Hsu, A. Goodrich, and R. Noufi, Co-evaporated $Cu_2ZnSnSe_4$ films and devices, Sol. Energy Mater. Sol. Cells **101**, 154 (2012).

[9] N. Vora, J. Blackburn, I. Repins, C. Beall, B. To, J. Pankow, G. Teeter, M. Young, and R. Noufi, Phase identification and control of thin films deposited by co-evaporation of elemental Cu, Zn, Sn, and Se, J. Vac. Sci. Technol. A **30**, 051201 (2012).

[10] M. Altosaar, J. Raudoja, K. Timmo, M. Danilson, M. Grossberg, J. Krustok, and E. Mellikov, $Cu_2Zn_{1-x}Cd_xSn(Se_{1-y}S_y)_4$ solid solutions as absorber materials for solar cells, Phys. Status Solidi A **205**, 167 (2008).

[11] P. Schöppe, G. Gurieva, S. Giraldo, G. Martínez-Criado, C. Ronning, E. Saucedo, S. Schorr, and C. S. Schnohr, Discrepancy between integral and local composition in off-stoichiometric $Cu_2ZnSnSe_4$ kesterites: A pitfall for classification, Appl. Phys. Lett. **110**, 043901 (2017).

[12] A. Khare, B. Himmetoglu, M. Johnson, D. J. Norris, M. Cococcioni, and E. S. Aydil, Calculation of the lattice dynamics and Raman spectra of copper zinc tin chalcogenides and comparison to experiments, J. Appl. Phys. **111**, 083707 (2012).

[13] M. Dimitrievska, A. Fairbrother, E. Saucedo, A. Pérez-Rodríguez, and V. Izquierdo-Roca, Influence of compositionally induced defects on the vibrational properties of device grade $Cu_2ZnSnSe_4$ absorbers for kesterite based solar cells, Appl. Phys. Lett. **106**, 073903 (2015).

[14] T. Gürel, C. Sevik, and T. Çağın, Characterization of vibrational, and mechanical properties of quaternary compounds Cu_2ZnSnS_4, and $Cu_2ZnSnSe_4$ in kesterite, and stannite structures, Phys. Rev. B **84**, 205201 (2011).

[15] M. Grossberg, J. Krustok, K. Timmo, and M. Altosaar, Radiative recombination in $Cu_2ZnSnSe_4$ monograins studied by photoluminescence spectroscopy, Thin Solid Films **517**, 2489 (2009).

[16] M. Grossberg, J. Krustok, J. Raudoja, K. Timmo, M. Altosaar, and T. Raadik, Photoluminescence and Raman study of $Cu_2ZnSn(Se_xS_{1-x})_4$ monograins for photovoltaic applications, Thin Solid Films **519**, 7403 (2011).

[17] A. Redinger, K. Hönes, X. Fontané, V. Izquierdo-Roca, E. Saucedo, N. Valle, A. Pérez-Rodríguez, and S. Siebentritt, Detection of a ZnSe secondary phase in coevaporated $Cu_2ZnSnSe_4$ thin films, Appl. Phys. Lett. **98**, 101907 (2011).

[18] H. Li, B. Wang, and L. Li, Study on Raman spectra of zinc selenide nanopowders synthesized by hydrothermal method, J. Alloys Compd. **506**, 327 (2010).

[19] J. Scott, T. Damen, W. Silfvast, R. Leite, and L. Cheesman, Resonant Raman scattering in ZnS and ZnSe with the cadmium laser, Opt. Commun. **1**, 397 (1970).

[20] C. Shan, Z. Liu, X. Zhang, C. Wong, and S. Hark, Wurtzite ZnSe nanowires: Growth, photoluminescence, and single-wire Raman properties, Nanotechnology **17**, 5561 (2006).

[21] V. V. Poborchii, A. V. Kolobov, and K. Tanaka, An *in situ* Raman study of polarization-dependent photocrystallization in amorphous selenium films, Appl. Phys. Lett. **72**, 1167 (1998).

[22] Q. Chen and Y. Zhang, The reversal of the laser-beam-induced-current contrast with varying illumination density in a $Cu_2ZnSnSe_4$ thin-film solar cell, Appl. Phys. Lett. **103**, 242104 (2013).

[23] R. Djemour, A. Redinger, M. Mousel, L. Gütay, X. Fontané, V. Izquierdo-Roca, A. Pérez-Rodríguez, and S. Siebentritt, The three *A* symmetry Raman modes of kesterite in $Cu_2ZnSnSe_4$, Opt. Express **21**, A695 (2013).

[24] M. Y. Valakh, V. Dzhagan, I. Babichuk, X. Fontane, A. Perez-Rodriquez, and S. Schorr, Optically induced structural transformation in disordered kesterite $Cu_2ZnSnSe_4$, JETP Lett. **98**, 255 (2013).

[25] K.-H. Kim and I. Amal, Growth of $Cu_2ZnSnSe_4$ thin films by selenization of sputtered single-layered Cu-Zn-Sn metallic precursors from a Cu-Zn-Sn alloy target, Electron. Mater. Lett. **7**, 225 (2011).

[26] X. Lin, J. Kavalakkatt, A. Ennaoui, and M. C. Lux-Steiner, $Cu_2ZnSn(S, Se)_4$ thin film absorbers based on ZnS, SnS and Cu_3SnS_4 nanoparticle inks: Enhanced solar cells performance by using a two-step annealing process, Sol. Energy Mater. Sol. Cells **132**, 221 (2015).

[27] T. Sekine, M. Izumi, T. Nakashizu, K. Uchinokura, and E. Matsuura, Raman scattering and infrared reflectance in 2H-$MoSe_2$, J. Phys. Soc. Jpn. **49**, 1069 (1980).

[28] Q. Chen, S. Bernardi, and Y. Zhang, Nondestructive high-power-high-temperature Raman spectroscopy for probing microscopic structural variations in CZTSe alloys, MRS Adv., DOI: (2017).

[29] F. Luckert, D. I. Hamilton, M. V. Yakushev, N. S. Beattie, G. Zoppi, M. Moynihan, I. Forbes, A. V. Karotki, A. V. Mudryi, M. Grossberg, J. Krustok, and R. W. Martin, Optical properties of high quality $Cu_2ZnSnSe_4$ thin films, Appl. Phys. Lett. **99**, 062104 (2011).

[30] M. Ishii, K. Shibata, and H. Nozaki, Anion distributions and phase transitions in $CuS_{1-x}Se_x$ ($x = 0$–1) studied by Raman spectroscopy, J. Solid State Chem. **105**, 504 (1993).

[31] B. Minceva-Sukarova, M. Najdoski, I. Grozdanov, and C. Chunnilall, Raman spectra of thin solid films of some metal sulfides, J. Mol. Struct. **410**, 267 (1997).

[32] C. M. Fella, A. R. Uhl, C. Hammond, I. Hermans, Y. E. Romanyuk, and A. N. Tiwari, Formation mechanism of $Cu_2ZnSnSe_4$ absorber layers during selenization of solution deposited metal precursors, J. Alloys Compd. **567**, 102 (2013).

[33] V. V. Poborchii, A. V. Kolobov, J. Caro, V. V. Zhuravlev, and K. Tanaka, Polarized Raman spectra of selenium species confined in nanochannels of $AlPO_{4-5}$ single crystals, Chem. Phys. Lett. **280**, 17 (1997).

[34] T. Gfroerer, Y. Zhang, and M. Wanlass, An extended defect as a sensor for free carrier diffusion in a semiconductor, Appl. Phys. Lett. **102**, 012114 (2013).

[35] M. Neuschitzer, Y. Sanchez, T. Olar, T. Thersleff, S. Lopez-Marino, F. Oliva, M. Espindola-Rodriguez, H. Xie, M. Placidi, V. Izquierdo-Roca, I. Lauermann, K. Leifer, A. Pérez-Rodriguez, and E. Saucedo, Complex surface chemistry of kesterites: Cu/Zn reordering after low temperature postdeposition annealing and its role in high performance devices, Chem. Mater. **27**, 5279 (2015).

[36] N. Yue, Y. Zhang, and R. Tsu, Ambient condition laser writing of graphene structures on polycrystalline SiC thin film deposited on Si wafer, Appl. Phys. Lett. **102**, 071912 (2013).

[37] J. He, S. N. Girard, M. G. Kanatzidis, and V. P. Dravid, Microstructure-lattice thermal conductivity correlation in nanostructured $PbTe_{0.7}S_{0.3}$ thermoelectric materials, Adv. Funct. Mater. **20**, 764 (2010).

[38] L. Su and Y. Zhang, Temperature coefficients of phonon frequencies and thermal conductivity in thin black phosphorus layers, Appl. Phys. Lett. **107**, 071905 (2015).

[39] Y. Dong, H. Wang, and G. S. Nolas, Synthesis and thermoelectric properties of Cu excess $Cu_2ZnSnSe_4$, Phys. Status Solidi RRL **8**, 61 (2014).

[40] K. Rudisch, Y. Ren, C. Platzer-Björkman, and J. Scragg, Order-disorder transition in *B*-type Cu_2ZnSnS_4 and limitations of ordering through thermal treatments, Appl. Phys. Lett. **108**, 231902 (2016).

[41] D. M. Többens, G. Gurieva, S. Levcenko, T. Unold, and S. Schorr, Temperature dependency of Cu/Zn ordering in CZTSe kesterites determined by anomalous diffraction, Phys. Status Solidi B **253**, 1890 (2016).

[42] J. J. Scragg, L. Choubrac, A. Lafond, T. Ericson, and C. Platzer-Björkman, A low-temperature order-disorder transition in Cu_2ZnSnS_4 thin films, Appl. Phys. Lett. **104**, 041911 (2014).